Earth-Science Reviews 257 (2024) 104903

Contents lists available at ScienceDirect

Earth-Science Reviews

journal homepage: www.elsevier.com/locate/earscirev

Quantifying the pattern of organic carbon burial through Cretaceous Oceanic Anoxic Event 2

Huifang Guo [a,b], Xi Chen [a,c,*], Hanwei Yao [a,c], Yinggang Zhang [d,e], Benjamin J.W. Mills [e], Kaibo Han [a,f], Shujuan Wu [a,c], Yida Yang [a,b], Zihao Wang [b], David B. Kemp [g]

[a] State Key Laboratory of Biogeology and Environmental Geology, China University of Geosciences, Beijing 100083, China
[b] School of Earth Sciences and Resources, China University of Geosciences, Beijing 100083, China
[c] Institute of Earth Sciences, China University of Geosciences, Beijing 100083, China
[d] Nanjing Institute of Geology and Palaeontology, Chinese Academy of Sciences, Nanjing, China
[e] School of Earth and Environment, University of Leeds, Leeds LS2 9JT, UK
[f] School of Earth Sciences, Hebei GEO University, Shijiazhuang 050031, China
[g] State Key Laboratory of Biogeology and Environmental Geology and Hubei Key Laboratory for Critical Zone Evolution, School of Earth Sciences, China University of Geosciences, Wuhan 430074, China

ARTICLE INFO

Keywords:
OAE 2
Cenomanian-Turonian
Tibet
Oceanic anoxia
Organic carbon burial

ABSTRACT

The Cenomanian-Turonian Oceanic Anoxic Event 2 (OAE 2, ca. 94 Ma) is characterized by a marked positive carbon isotope excursion (CIE) recorded in global marine basins. This CIE results from a global-scale increase in organic matter burial, facilitated by high productivity and seawater deoxygenation. To date, however, the precise pattern of changes in the burial rate of organic matter through the event has not been well constrained. In this work, we present a compilation of data from 42 globally distributed OAE 2 sites, as well as organic carbon isotope ($\delta^{13}C_{org}$), total organic carbon (TOC), and trace element concentration data from a new OAE 2 interval in southern Tibet, China. In southern Tibet, the absence of redox-sensitive trace element enrichment through OAE 2 indicates prevailing oxic conditions. Organic carbon (OC) mass accumulation rate (MAR) at this site decreased from the lower part of the CIE to the upper part, in contrast to an approximate doubling of organic carbon MAR in the upper part observed globally. This result, coupled with detailed analysis of the compilation, shows that redox was a key factor controlling organic burial rates during OAE 2, with OC MAR scaling positively with increasing deoxygenation. Leveraging a biogeochemical model to simulate these data suggests that 5–20% of the seafloor became anoxic during OAE 2, and that this deoxygenation was accompanied by 100% to 200% increase in global seawater P concentration. Our findings indicate that during OAE 2, elevated nutrient levels may have resulted from enhanced recycling from sediments under reducing conditions, sustaining intensified primary production and subsequent organic carbon export and burial.

1. Introduction

The Cretaceous Period witnessed elevated atmospheric CO_2 concentrations and temperatures, coinciding with episodic accumulation of organic carbon-rich sediments, known as oceanic anoxic events (OAEs; Schlanger and Jenkyns, 1976). OAEs marked prolonged and significant perturbations to the global carbon cycle (Schlanger et al., 1987; Takashima et al., 2006; Jenkyns, 2010; Herrle et al., 2015; Gambacorta et al., 2016; Owens et al., 2017), expressed by widespread deoxygenation across numerous ocean basins. OAEs are commonly distinguished stratigraphically by positive carbon isotope ($\delta^{13}C$) excursions (CIEs) related to globally enhanced burial of organic carbon enriched in ^{12}C (Kump, 1991; Jenkyns, 2010; Bryant et al., 2021). Oceanic Anoxic Event 2 (OAE 2), occurring around ~94 Ma, represents a peak of organic matter (OM) burial, and is associated with a CIE of approximately 2.5‰ in marine carbonates and up to 4‰ in marine OM (e.g., Jarvis et al., 2006; Tsandev and Slomp, 2009; Owens et al., 2018; Paez-Reyes et al., 2021; Papadomanolaki et al., 2022). The $\delta^{13}C$ profiles through OAE 2 in different basins share a similar basic pattern. Specifically, the $\delta^{13}C$ evolution can be divided into six distinct stages (Li et al., 2017), of which stages C3, C4 and C5 define the OAE 2 interval. In stages C1 and C6, the carbon isotope curve exhibits relative stability, representing pre- and

* Corresponding author at: State Key Laboratory of Biogeology and Environmental Geology, China University of Geosciences, Beijing 100083, China.
E-mail address: xichen@cugb.edu.cn (X. Chen).

https://doi.org/10.1016/j.earscirev.2024.104903
Received 16 March 2024; Received in revised form 16 August 2024; Accepted 19 August 2024
Available online 22 August 2024

post-event baseline values, respectively. Larger-scale and higher frequency $\delta^{13}C$ fluctuations characterize stage C2, with a relatively minor $\delta^{13}C$ negative shift sometimes observed. Stage C3 shows an initial rapid transition to higher $\delta^{13}C$ values ('build-up' phase), followed by a 'plateau' phase (stage C4) with relatively constant $\delta^{13}C$ values and finally a 'recovery' phase (stage C5), where $\delta^{13}C$ values return to near-pre-event values.

Different hypotheses have been proposed to elucidate the mechanisms of enhanced organic matter accumulation during OAE 2 (e.g., Jenkyns, 2010; Beil et al., 2020). These include the role of nutrient enrichment via emissions from large igneous provinces (LIPs) (Turgeon and Creaser, 2008; Trabucho Alexandre et al., 2010; Du Vivier et al., 2015; Schröder-Adams et al., 2019), remobilization from terrestrial areas due to marine transgressions (Jenkyns, 1980; Haq, 2014), input from intensified terrestrial weathering (Monteiro et al., 2012; Poulton et al., 2015; Jenkyns et al., 2017), and the release of phosphorus from sediments under benthic anoxic conditions (Mort et al., 2008; Wallmann, 2010; Beil et al., 2020). Understanding the triggers and mechanisms behind organic carbon enrichment during OAE 2 has significantly advanced in recent years (e.g., Schröder-Adams et al., 2019; Londoño and Collins, 2022). At the same time, previous studies have provided a robust estimate of the total organic carbon sequestration throughout the entire OAE 2 period, amounting to approximately 70 Eg (1 Eg = 10^{18} g), which exceeds the current marine carbon burial flux by more than two-fold (Owens et al., 2018). However, the variations in the organic carbon mass accumulation rates (OC MARs) across different CIE stages remain poorly understood, and the dominant drivers governing short-term organic carbon burial during the event also remain elusive. A key challenge in unraveling the driving forces and dynamics of OAE 2 is the uncertainties regarding its duration and the distinct stages it encompasses (Beil et al., 2020). The total duration of the CIE associated with OAE 2 has been previously estimated to have ranged from ~430 kyr to ~930 kyr (Sageman et al., 2006; Meyers et al., 2012; Ma et al., 2014; Eldrett et al., 2015; Li et al., 2017; Charbonnier et al., 2018; Gangl et al., 2019). A recent high-precision estimate of 619 kyr has been established cyclostratigraphically from site SH#1 in the USA (Jones et al., 2019). Discrepancies in previous timescale estimates are largely attributable to varied definitions of the onset and end of OAE 2. For example, some estimates are based on the stratigraphic pattern and magnitude of organic-enrichment, while others are based on the stratigraphic pattern of the CIE (Beil et al., 2020).

A robust understanding of OC MAR from globally distributed basins is a key prerequisite for understanding the precise pattern of global organic matter burial across OAE 2, and for interpreting the associated carbon isotope excursion. To date, however, only a few sites have been reported from the southern hemisphere and eastern Tethys Ocean. In this study, we have investigated the OC burial history and paleoenvironment during OAE 2 in the Qiangdong section, which was deposited on the southern margin of the eastern Tethys Ocean during the Cretaceous (Fig. 1 and S1). OAE 2 in this section has been identified by biostratigraphy (Jia et al., 2010) and low-resolution $\delta^{13}C_{org}$ curve (Zhang et al., 2016). We integrate these new data with previously published data from 42 globally distributed sites (Fig. 1) to assess the temporal pattern of OC MARs for different CIE stages at each site. Through this analysis, we establish a unified organic carbon burial rate curve for OAE 2, permitting precise comparison of OC MAR variations in a spatiotemporal context. In so doing, we investigate the drivers of short-term organic matter sequestration rates during OAE 2.

2. Materials and methods

2.1. Sample preparation and analysis in the Qiangdong section

In total, 72 samples with a spacing of 1 m were taken from the OAE interval (~72 m thick) of the Qiangdong section for organic carbon isotope and TOC analysis, and 37 samples with a spacing of 2 m were selected for major and trace element analyses. To prevent sampling of oxidized or contaminated material, weathered surfaces and visibly altered parts were trimmed off before grinding into a fine powder. The residual rock samples were crushed and ground to 200 mesh powder for

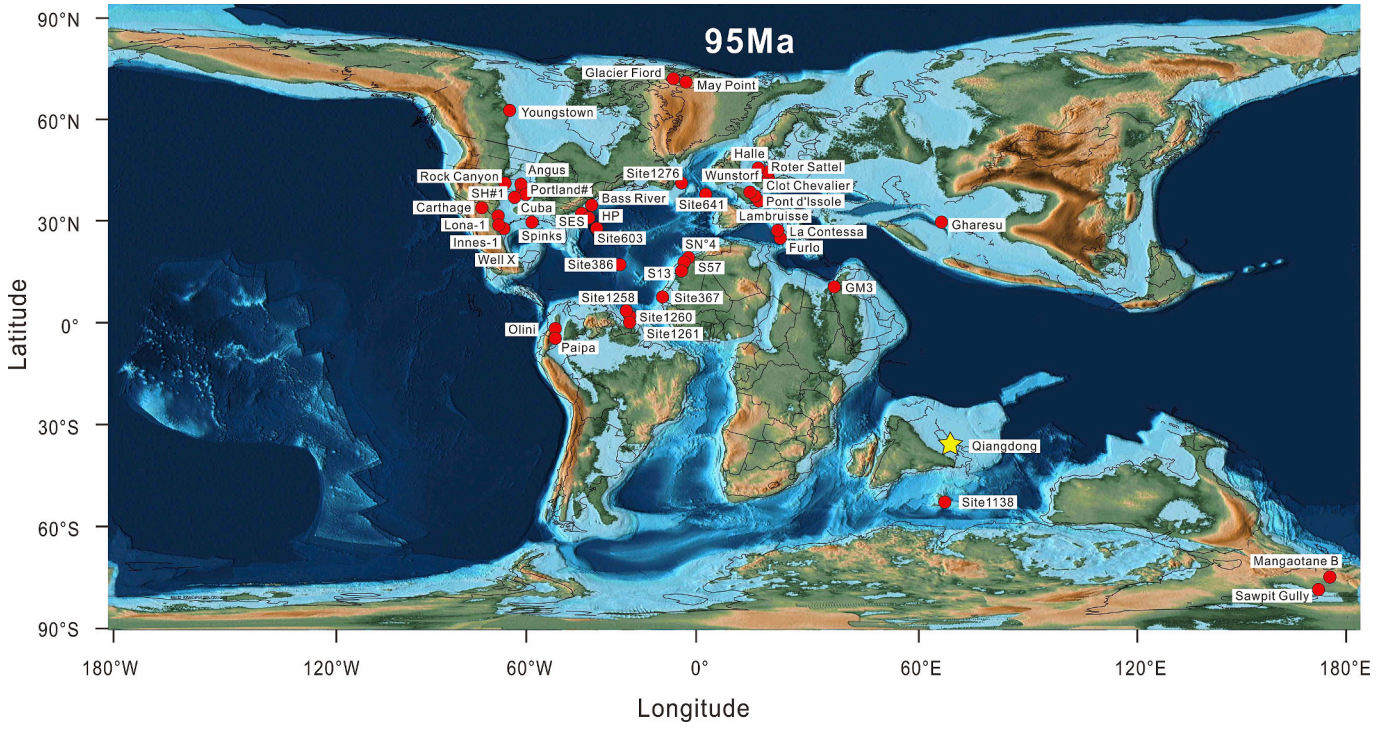

Fig. 1. Paleogeographic map (95 Ma, Cenomanian) and locations of OAE 2 sections (red dots). Referenced sources are detailed in Table 1. The yellow star marks the Qiangdong section. The map is adapted from the PALEOMAP Project (Scotese, 2016). (For interpretation of the references to colour in this figure legend, the reader is referred to the web version of this article.)

subsequent analysis. Methods used for the measurement of organic carbon isotopes, TOC, and major and trace element abundance are described in detail in the Supplementary Materials.

2.2. Data compilation and measurement of mass-accumulation rates

OAE 2 is one of the most widely documented carbon cycle perturbation events in the geological record (e.g., Bowman and Bralower, 2005; Jenkyns, 2010; Eldrett et al., 2017; Beil et al., 2018; Jones et al., 2021; Paez-Reyes et al., 2021; McDonald et al., 2022). We compiled data from 43 globally distributed OAE 2 sections that each clearly show the OAE 2 CIE, including the Qiangdong section (Fig. 1). Unlike the compilation approach of Owens et al. (2018), the selected sections only include those dominated by black shale facies, rather than carbonates, as previous studies have shown that carbonates typically have low TOC content. Following Kemp et al. (2022), we classify the redox state of each section, as reported in the literature, into three types: oxic-suboxic, suboxic-anoxic, and anoxic-euxinic. Detailed information on the compiled sections is provided in Table 1, with comprehensive information on the redox of each site provided in the Supplementary Materials Table S1.

The organic carbon burial rate during OAE 2 can be quantified for each of our studied sections using the available TOC data coupled with knowledge of rock density and bulk sediment accumulation rates. Hence, organic carbon mass accumulation rate (MAR; g/cm^2/kyr) is calculated by:

$$MAR[g/cm^2/kyr] = LSR\ [cm/kyr] \times \rho\ [g/cm^3] \times TOC\ [wt\%].$$

where LSR is the linear sedimentation rate, and ρ is rock density. Few rock density data have been previously published, and we assume instead (following Owens et al., 2018) a constant density of 2.4 g/cm^3, which is lower than the typical mudstone density of ~2.7 g/cm^3 since organic-rich rocks have generally lower density. In any case, the exact density value chosen has only a limited effect on the absolute MAR values calculated, and has no effect on calculations of changes in organic carbon burial rate.

The linear sedimentation rates for each section are calculated by

Table 1
The list of sites studied in this study, including data on stratigraphic thickness, organic carbon burial rates, and inferred redox, along with references. Question marks denote uncertain redox interpretation. The locations of the sites are shown in Fig. 1. WIS: Western Interior Seaway.

Site No.	Area	Study site	Thickness (m)	OC MAR (g/cm^2/kyr)	Redox interpretation	Reference (duration from)	Reference (data from)
1	USA (WIS)	Carthage	22.00	0.05	Suboxic-anoxic	Jones et al. (2019)	Bryant et al. (2021)
2	USA (WIS)	Iona-1 Core	18.03	0.11	Anoxic-euxinic	Eldrett et al. (2017)	Eldrett et al. (2015)
3	USA (WIS)	SH#1 Core	17.47	0.07	Anoxic-euxinic	Jones et al. (2019)	Jones et al. (2019)
4	USA (WIS)	Portland#1	7.99	0.03	Suboxic-anoxic	Eldrett et al. (2017)	McDonald et al. (2022)
5	USA (WIS)	Angus Core	11.39	0.09	Anoxic-euxinic	Jones et al. (2021)	Jones et al. (2021)
6	USA (WIS)	Cuba, Kansas	3.27	0.05	Suboxic-anoxic	Jones et al. (2019)	Bowman and Bralower (2005)
7	USA (WIS)	Rock Canyon	7.00	0.02	Anoxic-euxinic	Jones et al. (2019)	Bowman and Bralower (2005)
8	USA (WIS)	Innes-1 Core	12.04	0.06	Anoxic-euxinic	Eldrett et al. (2017)	Eldrett et al. (2017)
9	USA (WIS)	Well "X" core	17.65	0.09	Suboxic-anoxic	Eldrett et al. (2017)	Eldrett et al. (2017)
10	Canada (WIS)	Youngstown	14.40	0.36	Anoxic-euxinic?	Jones et al. (2019)	Prokoph (2001)
11	High Canadian Arctic	May Point	12.00	0.22	Anoxic-euxinic	Jones et al. (2019)	Lenniger et al. (2014)
12	High Canadian Arctic	Glacier Fiord	21.40	0.44	Suboxic-anoxic	Jones et al. (2019)	Schröder-Adams et al. (2019)
13	Gulf of Mexico	Spinks Core	14.87	0.11	Suboxic-anoxic	Jones et al. (2019)	Lowery et al. (2017)
14	USA (North Atlantic)	HP core	19.42	0.04	Suboxic-anoxic	Jones et al. (2019)	Lowery et al. (2021)
15	USA (North Atlantic)	SES core	10.82	0.04	Anoxic-euxinic?	Jones et al. (2019)	Lowery et al. (2021)
16	USA (North Atlantic)	Bass River	14.65	0.06	Oxic-suboxic	Jones et al. (2019)	van Helmond et al. (2014a)
17	Colombia (North Atlantic)	Paipa	11.90	0.27	Suboxic-anoxic	Paez-Reyes et al. (2021)	Paez-Reyes et al. (2021)
18	Colombia (North Atlantic)	Olini	6.05	0.12	Suboxic-anoxic	Paez-Reyes et al. (2021)	Paez-Reyes et al. (2021)
19	Demerara Rise (North Atlantic)	ODP Site 1260	1.60	0.03	Anoxic-euxinic	Eldrett et al. (2017)	Forster et al. (2007)
20	Demerara Rise (North Atlantic)	ODP Site 1258	4.68	0.27	Anoxic-euxinic	Jones et al. (2019)	Erbacher et al. (2005)
21	Demerara Rise (North Atlantic)	ODP Site 1261	9.13	0.26	Anoxic-euxinic	Eldrett et al. (2017)	Erbacher et al. (2005)
22	Morocco (North Atlantic)	S57	17.72	0.59	Anoxic-euxinic	Jones et al. (2019)	Tsikos et al. (2004)
23	Morocco (North Atlantic)	SN°4	41.94	1.30	Anoxic-euxinic	Beil et al. (2018)	Beil et al. (2018)
24	Morocco (North Atlantic)	S13	44.57	1.90	Anoxic-euxinic	Jones et al. (2019)	Kuypers et al. (2002)
25	North Atlantic	DSDP Site 367	5.60	0.94	Anoxic-euxinic	Jones et al. (2019)	Dickson et al. (2016)
26	North Atlantic	DSDP Site 386	6.38	0.18	Anoxic-euxinic	Jones et al. (2019)	van Helmond et al. (2014b)
27	North Atlantic	DSDP Site 603	5.03	0.10	Anoxic-euxinic	Jones et al. (2019)	van Helmond et al. (2014b)
28	North Atlantic	DSDP Site 641	1.09	0.01	Anoxic-euxinic	Jones et al. (2019)	van Helmond et al. (2014b)
29	North Atlantic	ODP Site 1276	3.97	0.05	Suboxic-anoxic	Jones et al. (2019)	Westermann et al. (2014)
30	France (Western Tethys)	Pont d'lssole	15.85	0.04	Suboxic-anoxic	Jones et al. (2019)	Jarvis et al. (2011)
31	France (Western Tethys)	Lambruisse	15.20	0.05	Suboxic-anoxic	Jones et al. (2019)	Danzelle et al. (2020)
32	France (Western Tethys)	Clot Chevalier	19.85	0.08	Suboxic-anoxic	Jones et al. (2019)	Gale et al. (2019)
33	Germany (Western Tethys)	Wunstorf	14.38	0.03	Suboxic-anoxic	Jones et al. (2019)	Du Vivier et al. (2014)
34	Germany (Western Tethys)	Halle	9.37	0.02	Anoxic-euxinic?	Jones et al. (2019)	Voigt et al. (2007)
35	Italy (Western Tethys)	La Contessa	0.72	0.02	Anoxic-euxinic	Jones et al. (2019)	Westermann et al. (2014)
36	Italy (Western Tethys)	Furlo	1.04	0.03	Anoxic-euxinic	Jones et al. (2019)	Westermann et al. (2014)
37	Jordan (Western Tethys)	GM3 CTB	15.14	0.04	Suboxic-anoxic	Jones et al. (2019)	Sepúlveda et al. (2009)
38	Switzerland (Western Tethys)	Roter Sattel	3.52	0.02	Anoxic-euxinic	Charbonnier et al. (2018)	Charbonnier et al. (2018)
39	Pacific Ocean	Sawpit Gully	33.44	0.02	Oxic-suboxic	Gangl et al. (2019)	Gangl et al. (2019)
40	Pacific Ocean	Mangaotane B	10.92	0.01	Oxic-suboxic	Gangl et al. (2019)	Gangl et al. (2019)
41	Indian Ocean	ODP Site 1138	2.22	0.04	Anoxic-euxinic	Jones et al. (2019)	Dickson et al. (2017)
42	Iran (Eastern Tethys)	Gharesu	33.50	0.06	Oxic-suboxic	Jones et al. (2019)	Kalanat et al. (2018)
43	China (Eastern Tethys)	Qiangdong	23.00	0.03	Oxic-suboxic	Jones et al. (2019)	This study

using the reported CIE stratigraphic thickness and the estimated duration of the CIE interval. As noted in Section 1, this duration of OAE 2 has been previously estimated using different methods (Sageman et al., 2006; Meyers et al., 2012; Ma et al., 2014; Eldrett et al., 2015; Li et al., 2017; Charbonnier et al., 2018; Gangl et al., 2019; Jones et al., 2019). In this study, we use the published timescales for each section, if available. If the duration was not previously published, we adopt a duration of 619 kyr, based on the astronomically tuned OAE 2 duration obtained recently from site SH#1, USA (Jones et al., 2019). Importantly, this timescale provides estimated durations for the different stages of the CIE: 193 kyr for stage C3, 324 kyr for stage C4 and 102 kyr for stage C5 (Jones et al., 2019). The stratigraphic thickness of the OAE 2 interval and individual stages in each section was defined by the available organic carbon isotope data and assumes unchanging sedimentation rate and no major stratigraphic gaps.

2.3. Earth system modeling

The Spatial Continuous Integration (SCION) model was used to explore potential mechanisms for organic matter burial and their links to climatic and environmental changes during OAE 2. SCION is a global biogeochemical model that integrates 3D spatial climate information from FOAM (Fast Ocean-Atmosphere Model; Goddéris et al., 2014) with the biogeochemical processes outlined in COPSE (Carbon-Oxygen-Phosphorus-Sulfur-Evolution) to predict the evolution of seawater chemistry over the entire Phanerozoic (Mills et al., 2021; Zhang et al., 2023). Validations of the model and detailed model descriptions are provided in Mills et al. (2021) and Zhang et al. (2023). The full model code and derivation are available at https://github.com.bjwmills/SCION.

With external forcings (e.g., degassing rate) fixed at 95 Ma, the SCION model inform a steady-state preceding OAE 2. With this steady-state, the riverine input of the key limiting nutrient phosphorus (P) is artificially set to increase by scaled with a time-dependent factor during the OAE 2 interval. This single forcing drives fluctuations in the seawater P reservoir and additional organic cabron burial. The artificially altering P input fluxes in the model are not as realistic as employing fully dynamic modeling, however, they can help focus our understanding of the likely phosphorus cycling involved during OAE 2 and relationships between this, the organic carbon burial record, and the responses of redox changes in the water column. Except for these revisions in the SCION model, carbon isotope fractionation factor for photosynthesis is fixed at − 27‰. This factor, within the range of −25‰ to −35‰ used previously in the model (Mills et al., 2021), was obtained from comparisons between our analyzed organic C isotope composition and previously reported inorganic C isotope composition.

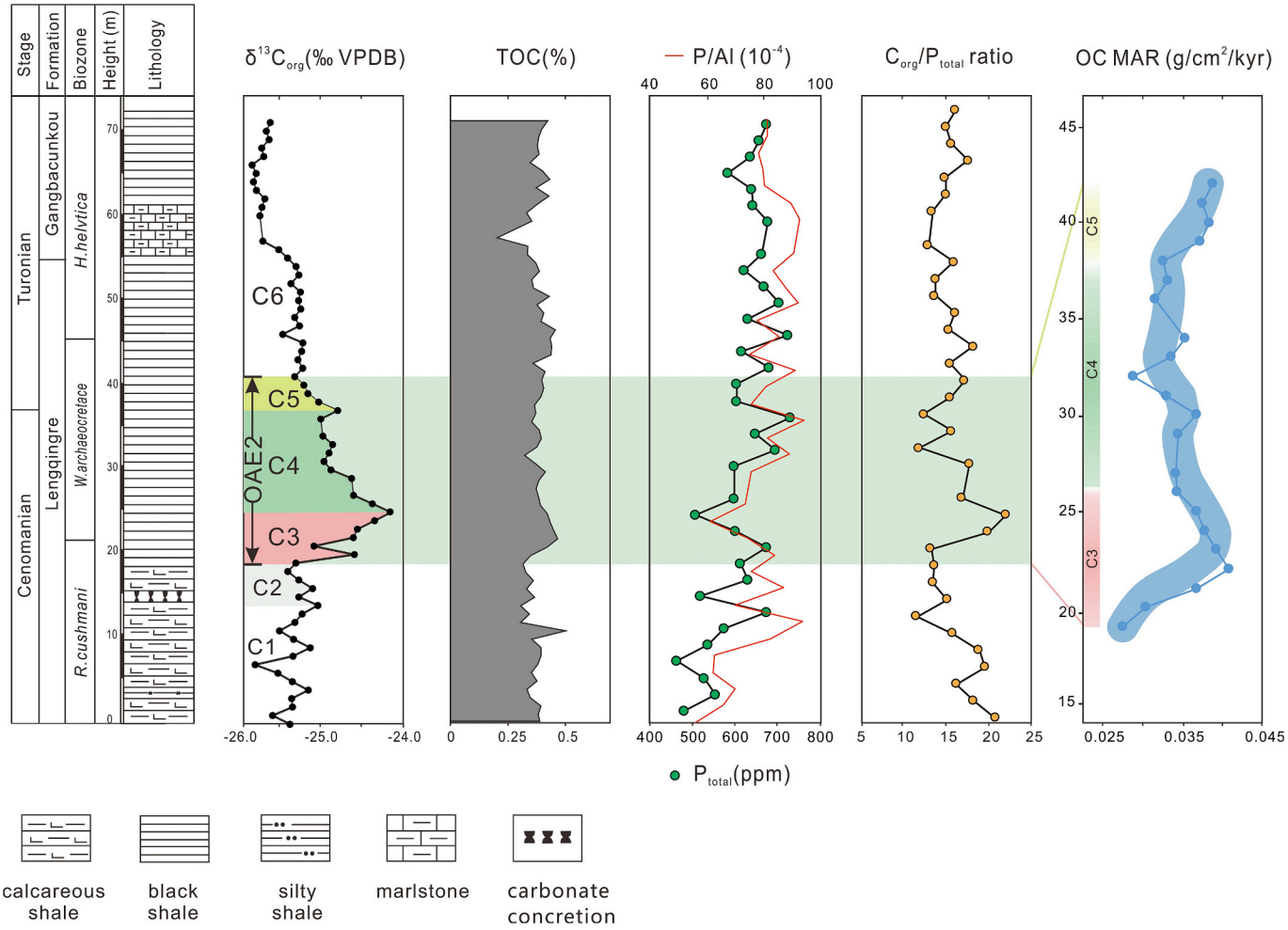

Fig. 2. Stratigraphic succession, carbon isotope composition, TOC content, Phosphorus contents, P/Al, atomic C_{org}:P_{tot} ratios and organic carbon burial rate (OC MAR) through the Qiangdong section. The light green shaded area represents the OAE 2 interval. The subdivisions of OAE 2 (stages C1-C6) are from Li et al. (2017). Blue bands show trends based on three-point average of the OC MAR data. (For interpretation of the references to colour in this figure legend, the reader is referred to the web version of this article.)

3. Results

3.1. Paleoenvironment and OC MAR variations across OAE 2 in the Qiangdong section

3.1.1. Organic carbon isotopes

Bulk organic carbon isotopes ($\delta^{13}C_{org}$) of the Qiangdong section range from − 26.50‰ to − 24.27‰ (Fig. 2), which is consistent with previous studies in this area (Jia et al., 2010; Zhang et al., 2016). A large positive $\delta^{13}C_{org}$ excursion between 20 m and 42 m is identified as OAE 2 based on the regional and global comparable variations in lithology, $\delta^{13}C$, and foraminiferal biostratigraphy (Wang et al., 2001; Wan et al., 2003; Jarvis et al., 2006; Li et al., 2006; Zhang et al., 2016).

In our study, the use of high-resolution sampling allows more precise identification of the different carbon isotope stages (C1-C6) compared to previous work (Zhang et al., 2016). At the base of the Qiangdong section, a segment with relatively stable $\delta^{13}C_{org}$ values is apparent (stage C1, ~0–17 m), with values varying between − 25.51‰ to − 24.94‰ (mean − 25.16‰). Stage C2 (17–20 m) is marked by a small-scale negative $\delta^{13}C_{org}$ excursion (~0.27‰), which was not previously recognised in this section (Zhang et al., 2016). Subsequently, $\delta^{13}C_{org}$ increases gradually from − 25.14‰ to − 24.27‰ (stage C3, 20–26 m), interrupted by a brief negative shift (Fig. 2). The end of stage C3 is at ~26 m, where $\delta^{13}C_{org}$ reached a maximum value (− 24.27‰). Within the subsequent plateau phase (stage C4, 26–38 m), $\delta^{13}C_{org}$ values are around − 24.80‰ with several small peaks and troughs <0.5‰ in magnitude. Thereafter, the recovery phase (stage C5, 38–42 m) encompasses a marked decrease in $\delta^{13}C_{org}$ to a stable value of − 25.12‰. The end of this stage marks the termination of the CIE. Above this, $\delta^{13}C_{org}$ is broadly stable (stage C6), through decreases again at around 57 m height (Fig. 2).

3.1.2. TOC and OC MAR variation

The total organic carbon (TOC) content of the Qiangdong section varies between 0.20 wt% and 0.50 wt% (Fig. 2). The most distinctive feature of the TOC profile is that the values fluctuate between 0.30 wt% and 0.45 wt% for the majority of the record, and is broadly stable except for some minor and transient positive and negative shifts.

The pre-OAE 2 interval (C1 and C2) generally exhibits low TOC content (<0.40 wt%), except for a single sample at 11 m with a value of 0.50 wt%. At the base of stage C3, TOC content increases slightly and is followed by an interval of relatively constant TOC of ~0.4 wt‰ throughout the stage C3. However, the OC MARs increase rapidly to 0.04 (g/cm^2/kyr) in the lower part of stage C3 and then decrease gradually in the upper part of this stage (Fig. 2). TOC values of ~0.4 wt‰ persist throughout the remainder of the section and are interrupted by a small decrease at ~57 m. In stage C4, OC MARs maintain low levels, with minor fluctuations around 0.03 g/cm^2/kyr (except for a low value), followed by a small increase during stage C5 (Fig. 2).

3.1.3. Phosphorus content and C_{org}: P_{tot} ratios

Total phosphorus (P_{tot}) concentrations in the Qiangdong section vary between 450 ppm and 750 ppm (Fig. 2). When normalized against Al, the trend in P_{tot}/Al correlates very well with the P_{tot} variations, strongly suggesting that P_{tot} variations are independent of lithological changes. The pre-OAE 2 interval (stages C1 and C2) is characterized by relatively variable but progressively increasing P_{tot} and P_{tot}/Al. Above this, P_{tot} decreases to 509 ppm through stage C3 and the start of stage C4 in the OAE 2 interval, and there is also a corresponding minima reached in P_{tot}/Al. P_{tot} and P_{tot}/Al increase again through most of stage C4. P_{tot} and P_{tot}/Al values in stage C5 and above the CIE to the top of the studied succession are broadly stable. As such, P content does not show any clear change at the termination of OAE 2.

C_{org}/P_{tot} ratios have been proposed as a reliable indicator of seafloor redox conditions in marine environments (Algeo and Ingall, 2007; Mort et al., 2008; Kraal et al., 2010; Beil et al., 2020). The C_{org}/P_{tot} ratio in the Qiangdong section mirrors the trend in P_{tot} (Fig. 2). C_{org}/P_{tot} in the strata below OAE 2 show a stepwise decreasing trend. Stage C3 is characterized by a sharp increase from ~13 to ~22. C_{org}/P_{tot} then gradually decreases to a minimum of ~12 during stage C4 and increases slightly during stage C5. Above stage C5, C_{org}/P_{tot} returns to relatively stable background values, with an average of 15.3.

3.1.4. Trace element record

The enrichment or depletion of redox-sensitive trace elements (RSTEs) in sediments depends on the availability of oxidants, making them useful indicators for deciphering the paleo-redox conditions related to organic-rich sediments (Brumsack, 2006; Tribovillard et al., 2006; Turgeon and Brumsack, 2006). Mo, V and U are generally show enrichment under O_2-depleted conditions. In addition, these elements have minimal terrigenous sources, and are thus considered as robust proxies for the assessment of seawater redox conditions (Tribovillard et al., 2006; Algeo and Tribovillard, 2009). Cu, Ni and Ba are micronutrients and are consequently widely employed as palaeoproductivity indicators. Raw and Al-normalized RSTE data from the Qiangdong section are shown in Fig. 3.

The concentrations of Mo are exceptionally low in the Qiangdong section, with almost all the data falling close to the detection limit of our analysis (~0.5 ppm). These Mo/Al values are well below that of average shale. U concentrations are also low, with all U/Al values below those of average shale. In contrast to Mo and U, V/Al values are higher than average shale and values are stable through the studied succession.

No enrichments of Cu and Ba are observed across the section, with all Al-normalized values remaining broadly stable and significantly below average shale values. Ni/Al values are close to those of average shale.

3.2. Global record of OC MARs during OAE 2

Our compilation of 43 global sections (including Qiangdong) comprises sections that have been extensively studied in biostratigraphy and carbon isotopic stratigraphy (Fig. 1). As such, the stratigraphic framework of the sections is well constrained, with well-defined C/T boundaries and biostratigraphic zonation schemes. Ages obtained through astronomical tuning of the OAE 2 interval thus allow high-resolution calculation of the OC MARs for the different substages. The average OC MAR values determined for each site span from 0.01 to 1.9 g/cm^2/kyr during OAE 2 (Fig. 4). Regions of inferred upwelling (e.g., Morocco) exhibit the highest values. Among the 43 sections, 39 localities have average OC MAR values <0.5 g/cm^2/kyr (including Qiangdong). Specifically, the majority of sites located in the WIS have organic carbon burial rates between 0.05 and 0.1 g/cm^2/kyr, while most sites in Tethys exhibit organic carbon burial rates below 0.05 g/cm^2/kyr.

Based on the compiled data from the 43 sites, we also generated a curve of mean OC MAR values in each stage of OAE 2 by employing bootstrap resampling (20,000 times) to ascertain the average value for each stage along with the 1-sigma standard deviation (Fig. 5). The bootstrap method mitigates the risk of over-reliance on individual data points (Singh and Xie, 2008). A mean value of 0.05 g/cm^2/kyr, as determined in previous studies, was regarded as the background value for stages C1–2 and C6 (Owens et al., 2018). The results show that the OC MAR during stage C3 (0.109 g/cm^2/kyr) is twice that of the background value. In stage C4, this rate (0.224 g/cm^2/kyr) increases to four times the background level. Notably, the burial rate in stage C5 (0.215 g/cm^2/kyr) is comparable to that observed in stage C4 (Fig. 5; Table 2). Unlike most sites, however, in our Qiangdong section OC MAR during stage C3 is slightly higher than in stage C4 (Fig. 2). Here, the accumulation rates of organic carbon increase in the lower part of stage C3, reaching a maximum value of ~0.04 g/cm^2/kyr. Thereafter, the accumulation rates gradually decrease to relatively low values that persist throughout stage C4. Stage C5 shows a slight increase in OC MARs.

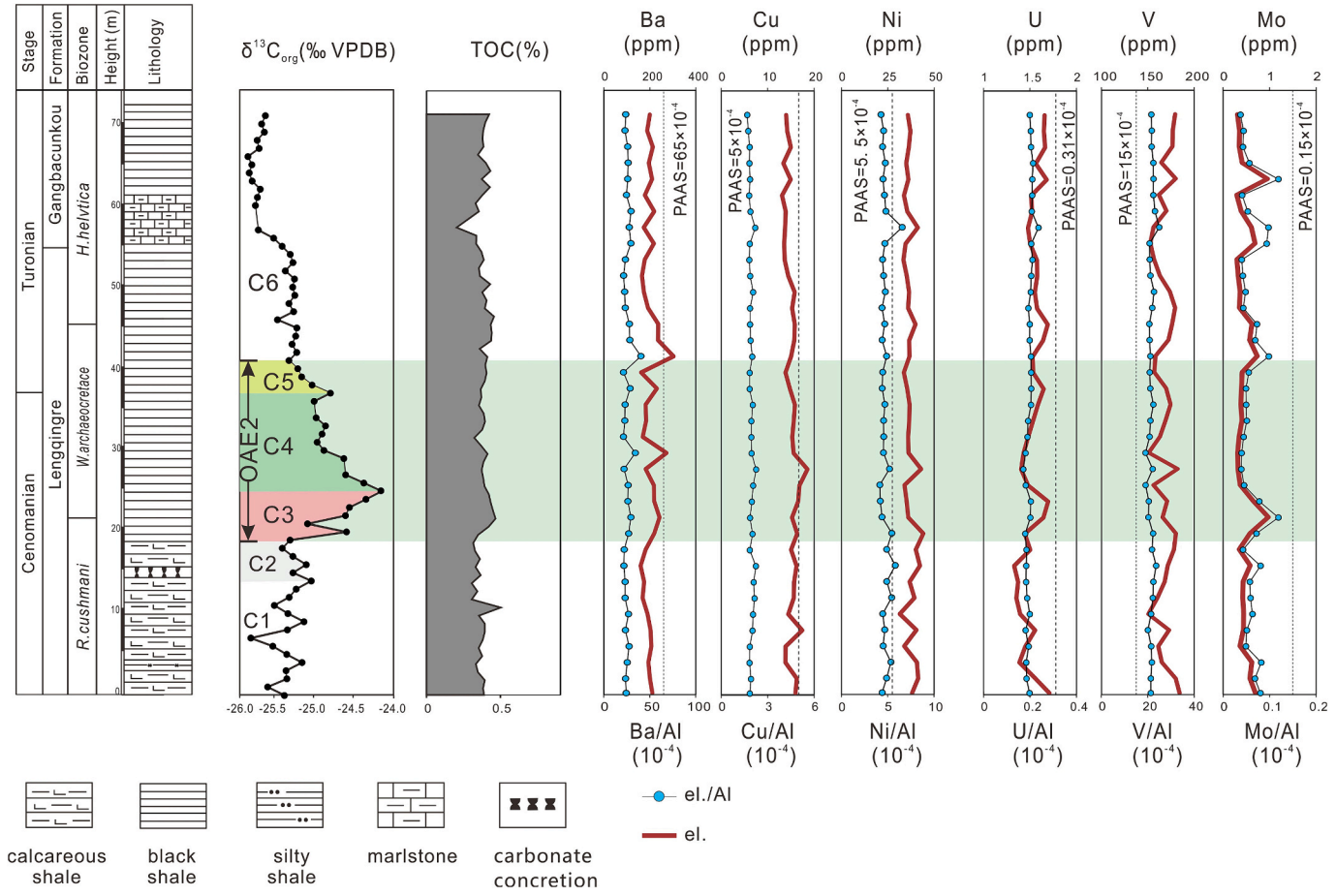

Fig. 3. Evolution of the redox-sensitive trace elements (RSTEs) (Mo, V, U), and elements associated with primary productivity (Ba, Cu, Ni) throughout the Qiangdong section. The red curves represent element concentrations, and the blue dots represent elements normalized to Al. The Al-normalized average shale values (post-Archean Australian shale, PAAS, dashed lines) are taken from Taylor and McLennan (1985). (For interpretation of the references to colour in this figure legend, the reader is referred to the web version of this article.)

4. Controls on organic enrichment during OAE 2

4.1. The role of seawater redox

Organic matter accumulation in marine environments is governed by the interplay of primary productivity, preservation conditions and dilution (e.g., Tessin et al., 2015; Lowery et al., 2021; Wang et al., 2021). Numerous studies have documented a covariance between redox sensitive trace elements (RSTEs, e.g., Mo, U, V) and TOC concentrations in ancient sediments and rocks (e.g., Algeo and Maynard, 2004; Tribovillard et al., 2006), thus supporting a link between redox conditions and organic carbon burial/preservation. In the Qiangdong section, there are no significant enrichments of TOC or RSTEs through the studied interval (Fig. 3; Fig. 6), indicating oxic conditions during OAE 2 on the shelf of East Tethys.

Redox conditions of the compiled sites during OAE 2 varied from oxic to euxinic (Table 1, see also Section 2.2). During OAE 2, the seafloor of the proto-North Atlantic Ocean was mainly anoxic-euxinic. In contrast, the seafloor of the Eastern Tethys and Pacific Oceans appear to have been dominantly oxic. The Western Interior Seaway (WIS) and Western Tethys were mainly suboxic-anoxic (Table 1).

The recorded redox states of different sites is typically evidenced by geochemical proxies, including Mo and U enrichments (Algeo and Maynard, 2004; Algeo and Tribovillard, 2009). In Fig. 6, we compiled available Mo—U data (quantified as enrichment factors) across OAE 2 from global basins (Fig. 6). The data emphasize the well-oxygenated condition in Qiangdong, the generally suboxic to anoxic conditions in the WIS (Portland-1 and Well "X" cores), the more severe reducing conditions (close to the anoxic/euxinic threshold) in the Iona-1 and Innes-1 cores, and the fully euxinic conditions in the Cape Verde Basin (ODP Site 367) and at Demerara Rise (ODP Site 1261).

We also used the method of bootstrap resampling (see Section 3.2) to create separate composite OC MAR curves across OAE 2 for sites with different redox states (Fig. 7). These data are presented in Table 2. The results show that OC MAR values are strongly dictated by the redox conditions at the studied sites (Fig. 7). The highest organic matter burial rates predominantly occur at anoxic-euxinic sites, with an average OC MAR of 0.27 g/cm^2/kyr during OAE 2. In contrast, oxic-suboxic areas have the lowest OC MAR, averaging at 0.04 g/cm^2/kyr. Suboxic-anoxic sites have an average OC MAR of 0.1 g/cm^2/kyr, relatively close to that of oxic-suboxic sites (Fig. 7). Numerous previous studies have also shown that there is a clear correlation between redox-sensitive elements (e.g., Mn, V/Cr) and organic carbon burial rate (e.g., ODP Site 1276, Westermann et al., 2014). This relationship underscores the influence of redox on organic carbon sequestration in marine sedimentary environments (e.g., Danzelle et al., 2018; Wang et al., 2021).

Redox state also played a key role in determining the changing magnitude in OC MAR through OAE 2 (Fig. 7). OC MAR values show the most substantial changes at anoxic-euxinic sites. Indeed, OC MAR in oxic-suboxic areas did not significantly change through OAE 2, and only a modest increase occurred at suboxic-anoxic sites. In order to describe the change of OC MARs during OAE 2, the average rates at stages C4 and C5 relative to C3 are denoted by the ratio (C4 + C5)/C3. Our compilation suggests that anoxic-euxinic sites (constituting ~58% of the studied

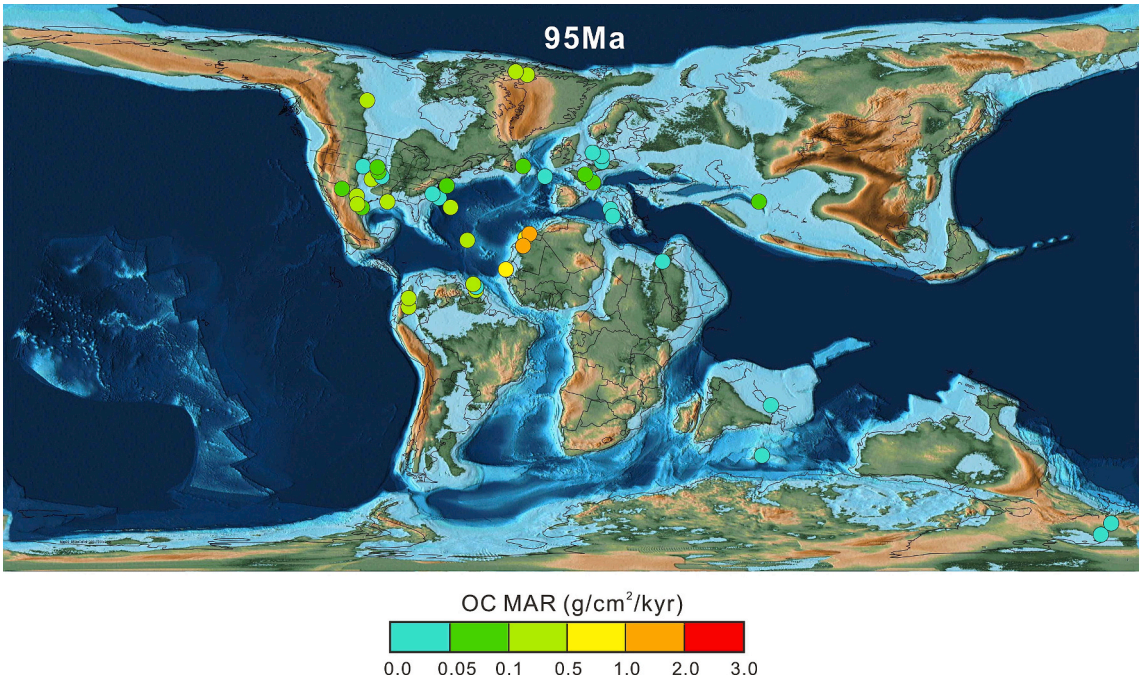

Fig. 4. Global pattern of calculated OC MAR for each site. Each coloured data point denotes data from a specific location with available high-resolution carbon isotope and TOC data (see also Table 1). The map is adapted from the PALEOMAP Project (Scotese, 2016).

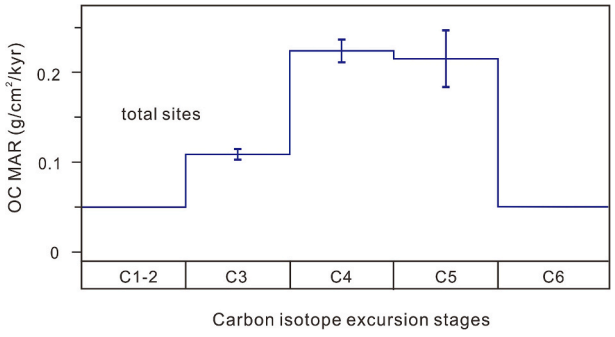

Fig. 5. Composite average value curve of all organic carbon burial rates (OC MARs) data for each stage of the OAE 2 CIE (stages C3-C5, with 1σ error bars) obtained by bootstrap resampling method, based on global compilation of all 43 sections. Stages C1–2 and C6 represent the pre- and post-event intervals, respectively, with OC MAR set to 0.05 g/cm^2/kyr in these intervals (see main text). Detailed data are shown in Table 2.

Table 2
Data on mean organic carbon burial rates in each stage of OAE 2, obtained by bootstrap resampling. See also Figs. 5 and 7, and main text for details.

Redox condition	Number of sites (n)	Stage C3		Stage C4		Stage C5	
		mean	1σ	mean	1σ	mean	1σ
Oxic-suboxic	5	0.042	0.002	0.034	0.001	0.041	0.005
Suboxic-anoxic	14	0.081	0.005	0.115	0.007	0.094	0.010
Anoxic-euxinic	24	0.139	0.011	0.327	0.026	0.337	0.062
Total sites	43	0.109	0.006	0.224	0.013	0.215	0.032

locations) exhibit an average (C4 + C5)/C3 ratio of 2.39 for OC MARs. Suboxic-anoxic sites (constituting ~30% of all sites) display a mean (C4 + C5)/C3 ratio of 1.29. The remaining ~12% of sites, categorized as oxic-suboxic, demonstrate a mean (C4 + C5)/C3 ratio of 0.89 (Fig. 7;

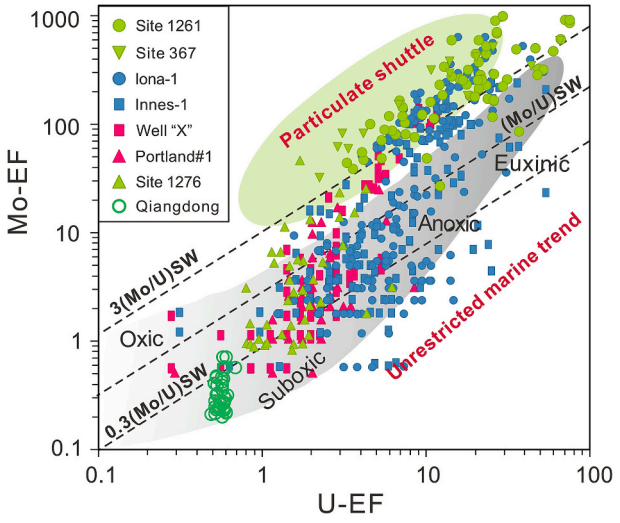

Fig. 6. Mo-EF (enrichment factor) versus U-EF for the Qiangdong section (this study), ODP Site 1261 and DSDP Site 367, Iona-1, Innes-1, Well "X", Portland#1 and Site1276. EF was calculated as $EF(X) = (X / Al)_{sample} / (X / Al)_{PAAS}$ (PAAS: post-Archean Australian shale, from Taylor and McLennan, 1985). Data sources are listed in Table 1. Diagonal dashed lines indicate the 3/1, 1/1 and 0.3/1 (Mo/U) ratios of present-day seawater. The area of gradient grey maps the Mo-EF vs. U-EF evolution under suboxic to euxinic conditions in modern unrestricted marine environments, as observed in eastern tropical Pacific sites (Tribovillard et al., 2012). The green area represents the "Particulate Shuttle" effect values, characteristic of weakly restricted basins (Tribovillard et al., 2012). (For interpretation of the references to colour in this figure legend, the reader is referred to the web version of this article.)

Table 2). A trend toward more reducing conditions during stages C4 and C5 of OAE 2 is indicated by high accumulation rates of redox-sensitive elements (Kolonic et al., 2005). Taken together, our analyses suggest that oxygen availability played an important role in controlling organic carbon burial during OAE 2. For sites deposited in shallow

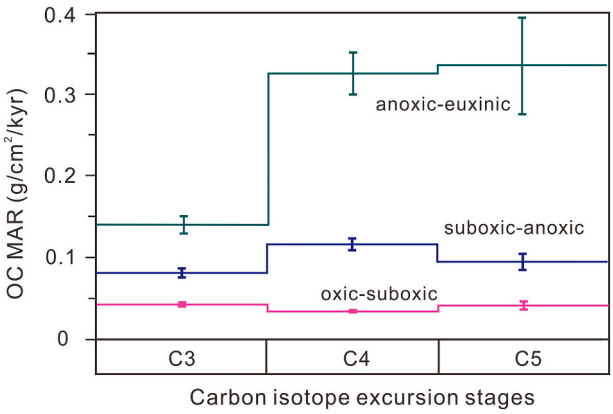

Fig. 7. Composite mean organic carbon burial rates (OC MAR) and associated 1σ uncertainties for sites with different redox environments (anoxic-euxinic, suboxic-anoxic, oxic-suboxic) in each stage of the OAE 2 CIE (stages C3-C5) obtained by bootstrap resampling, based on global compilation of all 43 sections. Detailed data are shown in Table 2.

well-oxygenated water (including the Qiangdong section) organic matter was nearly completely oxidized prior to burial. By contrast, anoxic to euxinic conditions would have diminished organic carbon remineralization rates and promoted organic carbon preservation and burial (e.g., Takashima et al., 2011; Westermann et al., 2014).

Our compilation confirms the correlation between OC MARs and redox conditions, but there is clear overlap in OC MAR values between different redox states (Table 1). This overlap can partly be attributed to the broad and overlapping redox classifications utilized. Moreover, diverse proxies employed for inferring OAE 2 redox vary in their efficacy and interpretation (e.g., Algeo and Liu, 2020). Different redox indicators may represent conditions in different parts of the sediment/water column (e.g., Hetzel et al., 2009). Additionally, redox interpretations can be equivocal, for example, black shales in the Tethyan Himalayas marked by low bioturbation but also low TOC content (Wang et al., 2001).

4.2. The role of nutrients and productivity

Previous studies have suggested that enhanced organic carbon sequestration at the onset of OAE 2 was likely initiated due to enhanced nutrient input sourced via Large Igneous Province emplacement (Du Vivier et al., 2014; Papadomanolaki et al., 2022), increased continental weathering and runoff (Blättler et al., 2011; Pogge von Strandmann et al., 2013; Van Helmond et al., 2015; Chen et al., 2021), and/or via hydrothermal alteration of basalts (Trabucho Alexandre et al., 2010). Benthic regeneration of nutrients could also have significantly contributed to sustaining primary productivity (e.g., Kuypers et al., 2002; Mort et al., 2008; Beil et al., 2020).

Phosphorus is the primary limiting nutrient controlling marine biological productivity on geological timescales (e.g., Rimmer et al., 2004; Paytan and McLaughlin, 2007; Schoepfer et al., 2015), and as such has the potential to mediate the occurrence of high-productivity events (e.g., Kuypers et al., 2002; Handoh and Lenton, 2003). The atomic C_{org}:P_{tot} ratio provides a proxy to assess seafloor oxygen content and the corresponding phosphorus retention ability of sediments (Algeo and Ingall, 2007; Kraal et al., 2010). Burial of phosphorus bound to iron oxides directly correlates with the mean oxygen concentration in the deep ocean (Komar and Zeebe, 2017). This means that less P is buried through P_{Fe} (i.e., more is regenerated) with decreasing oxygen levels, and P cannot be buried effectively in fully anoxic waters (Tsandev and Slomp, 2009; Komar and Zeebe, 2017). P remobilized from sediments would increase nutrient availability in the surface ocean, which in turn can promote intensified primary production and hence more oxygen consumption via organic matter respiration, thus creating a positive feedback loop.

In the Qiangdong section, C_{org}:P_{tot} ratios are significantly lower than the Redfield ratio (106:1; Redfield et al., 1963) and other productivity proxies (e.g., Ba, Ni and Cu) are not enriched (Fig. 3), indicating oligotrophic conditions. The sediments in the Qiangdong section were deposited in a well-oxygenated shallow marine environment, where P remobilization was clearly limited. Limited nutrient input could be responsible for the low OC MAR observed at Qiangdong and other oxic sites in the compilation. In oxygenated shallow marine systems, phosphorus availability is predominantly regulated by terrestrial fluxes and is directly utilized to sustain primary productivity (Ruttenberg, 2003). As noted earlier, OC MAR in Qiangdong is slightly higher in stage C3 than that observed in stages C4 and C5. This phenomenon could be because of higher nutrient fluxes from the continents due to enhanced weathering intensity during C3, as evidenced by zinc and lithium isotope data (e.g., Pogge von Strandmann et al., 2013; Chen et al., 2021).

For all 43 compiled sites, C_{org}:P_{tot} ratio data are available from 11 sections, covering diverse redox conditions. These data are from our Qiangdong section (oxic-suboxic), the North Atlantic (anoxic-euxinic) and WIS (suboxic-anoxic). A robust correlation between C_{org}:P_{tot} ratios and OC MAR at these sites is observed (Fig. 8). Therefore, at the sites where anoxic to euxinic conditions prevailed during OAE 2, high OC MAR in stages C4 and C5 likely resulted from the positive feedback loop of remobilization of phosphorus, which stimulated productivity and further facilitated anoxia. At sites characterized by relatively oxic conditions, there is no positive feedback mechanism for phosphorus, resulting in low C_{org}:P_{tot} ratio and diminished organic matter burial.

4.3. Quantifying nutrient influx during OAE 2

Enhanced nutrient influx and productivity has long been regarded as a probable trigger for OAEs generally and increased OC MAR (e.g., Jenkyns, 2003). However, the magnitude of nutrient input changes required through this mechanism is not well constrained quantitively. In this study, we modelled the inferred OC MAR changes during OAE 2 using the SCION model (Fig. 9). The seawater P reservoir size (Fig. 9A) was influenced by an artificial riverine nutrient P input forcing (or by altering P fluxes from sediment remobilization), to match the OC MAR records. When phosphorus inputs are set to rise in a two-stage pattern across stages C3 and C4 (Fig. 9A), the model yields an OC MAR curve that best fits with our empirically determined composite curve (Fig. 9B). To reproduce the maximum empirically determined OC MAR values in

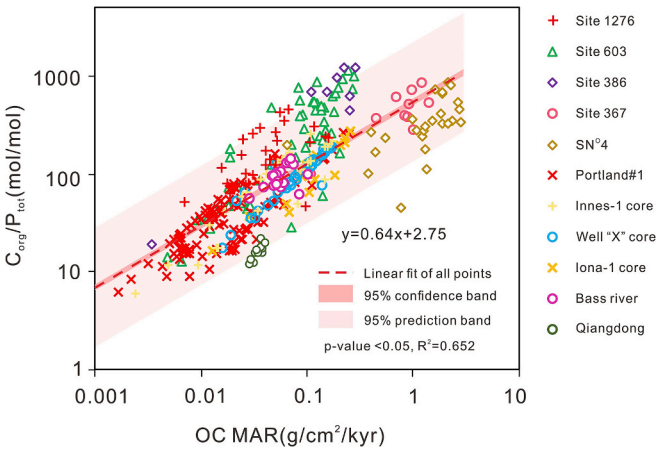

Fig. 8. Cross plot of OC MAR (g/cm^2/kyr) and C_{org}/P_{tot} (mol/mol) from 11 sites where the C_{org}:P_{tot} ratio data are available showing a significant positive correlation (R^2 = 0.652, *P*-value <0.05). The data sources for each point are shown in Table 1.

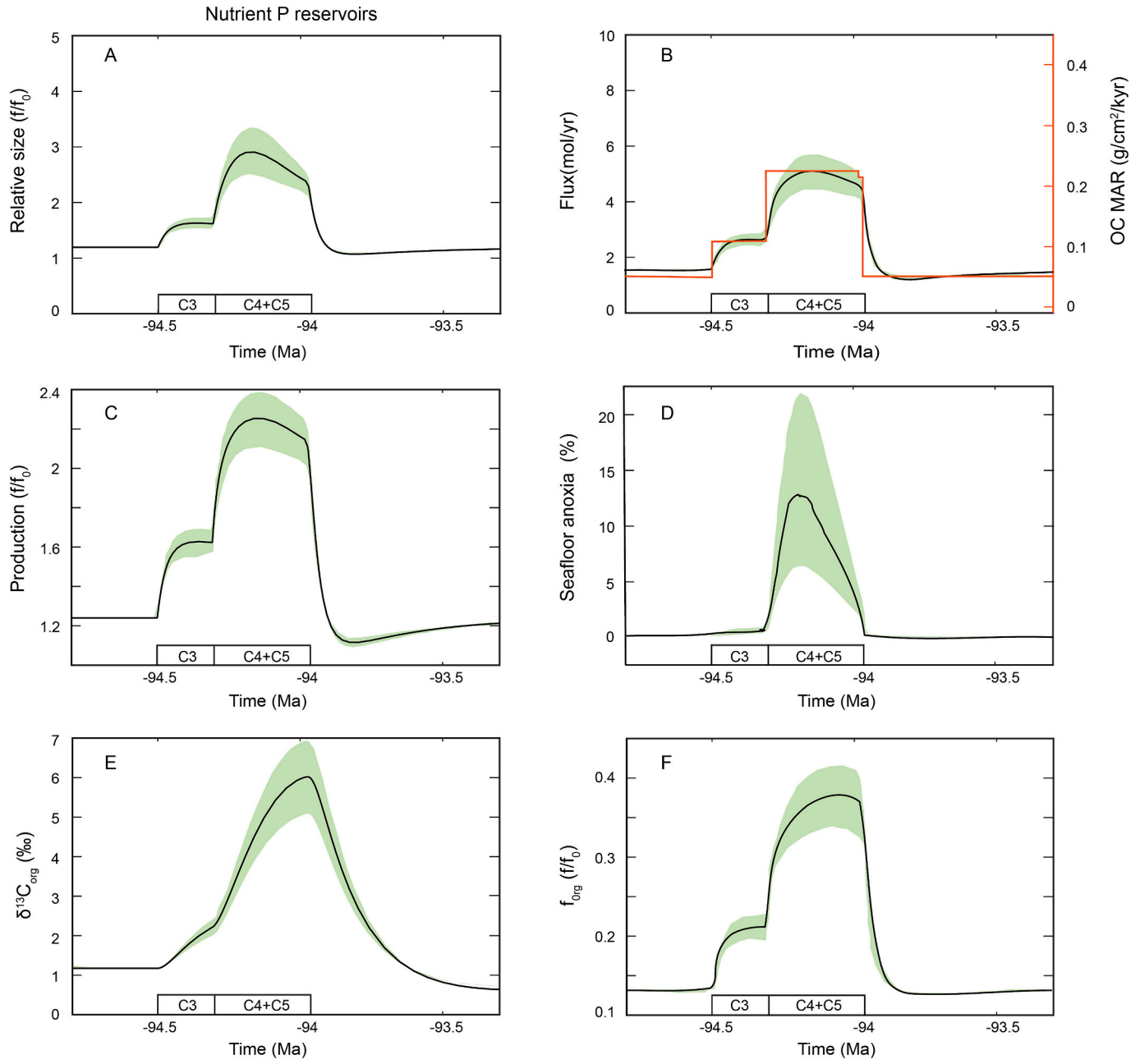

Fig. 9. SCION model outputs under a varying P input. The age model (horizontal axis) is estimated by assuming the durations of each phase and the starting age of the stage C3 at ~94.5 Ma. (A) Modelled ocean nutrient P reservoir size relative to modern level (f/f_0); (B) Modelled organic carbon burial rates (black line) and empirically determined OC MAR from our compilation (red line) (also shown in Fig. 4); (C) Modelled primary productivity relative to modern level (f/f_0); (D) Modelled seafloor anoxia (%); (E) $\delta^{13}C_{org}$ (‰); (F) Percentage of organic carbon in total carbon burial. Shaded green areas are the 20% uncertainties in the artificial P input and its effects on the modeling results. (For interpretation of the references to colour in this figure legend, the reader is referred to the web version of this article.)

C4 and C5, a ~ 140% (i.e. 2.4-fold) increase in P concentration is required relative to background values. The increase in OC MAR in stage C3 requires a more modest increase in P availability (~30% increase). In this scenario, the model also indicates a two-stage increase in primary productivity, ocean anoxia (quantified as an area percentage of anoxic seafloor) and a corresponding increase in the proportion of organic carbon buried (Fig. 9C, D and F). In detail, productivity during stages C4 and C5 underwent a 40% increase compared to stage C3 (Fig. 9C). Meanwhile, the increase in the modelled area of anoxic seafloor undergoes only a slight increase across the start of OAE 2 in stage C3. However, the modelled area of anoxic seafloor increases substantially in stages C4 and C5, and is ~24 times larger in stages C4 and C5 (~12%) compared to stage C3 (~0.5%) (Fig. 9D). This is consistent with previous work, corroborating the magnitude of oceanic anoxia expansion during stages C4 and C5 provided by previous geochemical studies using global redox proxies (e.g., sulfur isotope and uranium isotope) (Owens et al., 2013; Clarkson et al., 2018). These results indicate that intensified ocean anoxia coupled with enhanced productivity synergistically contributed to the elevated organic carbon burial observed in the stages C4 and C5, corroborating our findings discussed in Sections 4.1 and 4.2. The magnitude of the output $\delta^{13}C_{org}$ (~4–6‰) in our model is slightly higher than that observed in geological data (~3‰) (Papadomanolaki et al., 2022; Fig. 9E), with the shape also slightly differing from the geological record (Li et al., 2017). A possible explanation for the larger modelled

CIE amplitude could be the missing consideration of isotopically lighter carbon input, mainly from the LIP magmatisms and enhanced carbonate burial during the OAE 2, which would reduce the proportion of organic carbon output and the corresponding carbon isotope values. In addition, simply comparing the modelled marine organic carbon burial fluxes to the OC MAR record may lead to underestimate the varying degrees of loss of organic carbon after deposition. The model outputs are simply compared to the average record of OC MAR, which simplified our modeling strategy but neglected the possible existence of extremely high/low carbon burial in some intervals and could result in the mismatched $\delta^{13}C$ morphologies.

Our modeling results show that lower OC MAR in stage C3 compared to stages C4 and C5 could have resulted from a lower P reservoir size and lower productivity (Fig. 9A and C). It is noteworthy, however, that only the global average state of each CIE stage is modelled. Therefore, it is possible that some locally lower OC MAR in stage C3 than in stages C4 and C5 could have resulted from the reoxygenation of benthic water in the proto-Atlantic region during the upper part of stage C3, i.e. in the Plenus Cold Event (O'Connor et al., 2020).

5. Conclusions

In this study, we present new organic carbon isotope ($\delta^{13}C$), total organic carbon (TOC) and trace element concentrations from the Qiangdong section in southern Tibet, China. The absence of redox-sensitive trace element (RSTE) enrichments in this section suggests prevailing oxic conditions and relatively low productivity. Our analysis of this site and a global compilation of OAE 2 sites shows that anoxic-euxinic environments were associated with the most significant increases in organic carbon burial. Our study underscores the major influence of redox conditions on organic enrichment and burial rates. An observed positive correlation between C_{org}:P_{tot} ratios and OC MARs from our compiled sites suggests enhanced anoxia during stages C4 and C5 of OAE 2. Anoxia was likely driven and promoted by a positive feedback loop owing to increased remobilization of P from anoxic-euxinic sediments, which then further promoted and sustained productivity and oxygen consumption in the water column. Conversely, well-oxygenated environments lacked this feedback, leading to lower organic carbon burial rates in stages C4 and C5. Model simulations that reconstruct the observed OC MAR trends in our compiled data suggest that productivity during stages C4 and C5 underwent a 40% increase compared to stage C3, and that areal extent of anoxic seafloor during OAE 2 in stages C4 and C5 was approximately 24 times larger than in stage C3.

Declaration of competing interest

The authors declare that they have no known competing financial interests or personal relationships that could have appeared to influence the work reported in this paper.

Data availability

Data will be made available on request.

Acknowledgements

This work is financially supported by the National Natural Science Foundation of China (42050102), National Key Research and Development Program of China (2023YFF0804000) and Fundamental Research Funds for the Central Universities (2652023001). It contributes to IGCP 739.

Appendix A. Supplementary data

Supplementary data to this article can be found online at https://doi.org/10.1016/j.earscirev.2024.104903.

References

Algeo, T.J., Ingall, E., 2007. Sedimentary Corg: P ratios, paleocean ventilation, and Phanerozoic atmospheric pO2. Palaeogeogr. Palaeoclimatol. Palaeoecol. 256, 130–155. https://doi.org/10.1016/j.palaeo.2007.02.029.

Algeo, T.J., Liu, J., 2020. A re-assessment of elemental proxies for paleoredox analysis. Chem. Geol. 540, 119549 https://doi.org/10.1016/j.chemgeo.2020.119549.

Algeo, T.J., Maynard, J.B., 2004. Trace-element behavior and redox facies in core shales of Upper Pennsylvanian Kansas-type cyclothems. Chem. Geol. 206, 289–318. https://doi.org/10.1016/j.chemgeo.2003.12.009.

Algeo, T.J., Tribovillard, N., 2009. Environmental analysis of paleoceanographic systems based on molybdenum–uranium covariation. Chem. Geol. 268, 211–225. https://doi.org/10.1016/j.chemgeo.2009.09.001.

Beil, S., Kuhnt, W., Holbourn, A.E., Aquit, M., Flögel, S., Chellai, E.H., Jabour, H., 2018. New insights into Cenomanian paleoceanography and climate evolution from the Tarfaya Basin, southern Morocco. Cretac. Res. 84, 451–473. https://doi.org/10.1016/j.cretres.2017.11.006.

Beil, S., Kuhnt, W., Holbourn, A., Scholz, F., Oxmann, J., Wallmann, K., Lorenzen, J., Aquit, M., Chellai, E.H., 2020. Cretaceous oceanic anoxic events prolonged by phosphorus cycle feedbacks. Clim. Past 16, 757–782. https://doi.org/10.5194/cp-16-757-2020.

Blättler, C.L., Jenkyns, H.C., Reynard, L.M., Henderson, G.M., 2011. Significant increases in global weathering during Oceanic Anoxic events 1a and 2 indicated by calcium isotopes. Earth Planet. Sci. Lett. 309, 77–88. https://doi.org/10.1016/j.epsl.2011.06.029.

Bowman, A.R., Bralower, T.J., 2005. Paleoceanographic significance of high-resolution carbon isotope records across the Cenomanian–Turonian boundary in the Western Interior and New Jersey coastal plain, USA. Mar. Geol. 217, 305–321. https://doi.org/10.1016/j.margeo.2005.02.010.

Brumsack, H.-J., 2006. The trace metal content of recent organic carbon-rich sediments: implications for cretaceous black shale formation. Palaeogeogr. Palaeoclimatol. Palaeoecol. 232, 344–361. https://doi.org/10.1016/j.palaeo.2005.05.011.

Bryant, R., Leckie, R.M., Bralower, T.J., Jones, M.M., Sageman, B.B., 2021. Microfossil and geochemical records reveal high-productivity paleoenvironments in the Cretaceous Western Interior Seaway during Oceanic Anoxic Event 2. Palaeogeogr. Palaeoclimatol. Palaeoecol. 584, 110679 https://doi.org/10.1016/j.palaeo.2021.110679.

Charbonnier, G., Boulila, S., Spangenberg, J.E., Adatte, T., Föllmi, K.B., Laskar, J., 2018. Obliquity pacing of the hydrological cycle during the Oceanic Anoxic Event 2. Earth Planet. Sci. Lett. 499, 266–277. https://doi.org/10.1016/j.epsl.2018.07.029.

Chen, X., Sageman, B.B., Yao, H., Han, K., Zou, Y., Wang, C., 2021. Zinc isotope evidence for paleoenvironmental changes during cretaceous Oceanic Anoxic Event 2. Geology 49, 412–416. https://doi.org/10.1130/G48198.1.

Clarkson, M.O., Stirling, C.H., Jenkyns, H.C., Dickson, A.J., Porcelli, D., Moy, C.M., Pogge von Strandmann, P.A.E., Cooke, I.R., Lenton, T.M., 2018. Uranium isotope evidence for two episodes of deoxygenation during Oceanic Anoxic Event 2. Proc. Natl. Acad. Sci. 115, 2918–2923. https://doi.org/10.1073/pnas.1715278115.

Danzelle, J., Riquier, L., Baudin, F., Thomazo, C., Pucéat, E., 2018. Oscillating redox conditions in the Vocontian Basin (SE France) during Oceanic Anoxic Event 2 (OAE 2). Chem. Geol. 493, 136–152. https://doi.org/10.1016/j.chemgeo.2018.05.039.

Danzelle, J., Riquier, L., Baudin, F., Thomazo, C., Pucéat, E., 2020. Nitrogen and carbon cycle perturbations through the Cenomanian-Turonian oceanic anoxic event 2 (~94 Ma) in the Vocontian Basin (SE France). Palaeogeogr. Palaeoclimatol. Palaeoecol. 538, 109443 https://doi.org/10.1016/j.palaeo.2019.109443.

Dickson, A.J., Jenkyns, H.C., Porcelli, D., van den Boorn, S., Idiz, E., 2016. Basin-scale controls on the molybdenum-isotope composition of seawater during Oceanic Anoxic Event 2 (Late Cretaceous). Geochim. Cosmochim. Acta 178, 291–306. https://doi.org/10.1016/j.gca.2015.12.036.

Dickson, A.J., Saker-Clark, M., Jenkyns, H.C., Bottini, C., Erba, E., Russo, F., Gorbanenko, O., Naafs, B.D., Pancost, R.D., Robinson, S.A., 2017. A Southern Hemisphere record of global trace-metal drawdown and orbital modulation of organic-matter burial across the Cenomanian–Turonian boundary (Ocean Drilling Program Site 1138, Kerguelen Plateau). Sedimentology 64, 186–203. https://doi.org/10.1111/sed.12303.

Du Vivier, A.D., Selby, D., Sageman, B.B., Jarvis, I., Gröcke, D.R., Voigt, S., 2014. Marine 187Os/188Os isotope stratigraphy reveals the interaction of volcanism and ocean circulation during Oceanic Anoxic Event 2. Earth Planet. Sci. Lett. 389, 23–33. https://doi.org/10.1016/j.epsl.2013.12.024.

Du Vivier, A., Selby, D., Condon, D., Takashima, R., Nishi, H., 2015. Pacific 187Os/188Os isotope chemistry and U–Pb geochronology: Synchroneity of global Os isotope change across OAE 2. Earth Planet. Sci. Lett. 428, 204–216. https://doi.org/10.1016/j.epsl.2015.07.020.

Eldrett, J.S., Ma, C., Bergman, S.C., Lutz, B., Gregory, F.J., Dodsworth, P., Phipps, M., Hardas, P., Minisini, D., Ozkan, A., 2015. An astronomically calibrated stratigraphy of the Cenomanian, Turonian and earliest Coniacian from the cretaceous Western Interior Seaway, USA: Implications for global chronostratigraphy. Cretac. Res. 56, 316–344. https://doi.org/10.1016/j.cretres.2015.04.010.

Eldrett, J.S., Dodsworth, P., Bergman, S.C., Wright, M., Minisini, D., 2017. Water-mass evolution in the Cretaceous Western Interior Seaway of North America and equatorial Atlantic. Clim. Past 13, 855–878. https://doi.org/10.5194/cp-13-855-2017.

Erbacher, J., Friedrich, O., Wilson, P.A., Birch, H., Mutterlose, J., 2005. Stable organic carbon isotope stratigraphy across Oceanic Anoxic Event 2 of Demerara rise, western tropical Atlantic. Geochem. Geophys. Geosyst. 6, Q06010. https://doi.org/10.1029/2004GC000850.

Forster, A., Schouten, S., Moriya, K., Wilson, P.A., Sinninghe Damsté, J.S., 2007. Tropical warming and intermittent cooling during the Cenomanian/Turonian oceanic anoxic event 2: Sea surface temperature records from the equatorial Atlantic. Paleoceanography 22, PA1219. https://doi.org/10.1029/2006PA001349.

Gale, A.S., Jenkyns, H.C., Harilaos, T., van Breugel, Y., Sinninghe Damsté, J.S., Bottini, C., Erba, E., Russo, F., Falzoni, F., Petrizzo, M.R., 2019. High-resolution bio- and chemostratigraphy of an expanded record of Oceanic Anoxic Event 2 (late Cenomanian–early Turonian) at Clot Chevalier, near Barrême, SE France (Vocontian Basin). Newsl. Stratigr. 52, 97–129. https://doi.org/10.1127/nos/2018/0445.

Gambacorta, G., Bersezio, R., Weissert, H., Erba, E., 2016. Onset and demise of cretaceous oceanic anoxic events: the coupling of surface and bottom oceanic processes in two pelagic basins of the western Tethys. Paleoceanography 31, 732–757. https://doi.org/10.1002/2015PA002922.

Gangl, S.K., Moy, C.M., Stirling, C.H., Jenkyns, H.C., Crampton, J.S., Clarkson, M.O., Ohneiser, C., Porcelli, D., 2019. High-resolution records of Oceanic Anoxic Event 2: Insights into the timing, duration and extent of environmental perturbations from the palaeo-South Pacific Ocean. Earth Planet. Sci. Lett. 518, 172–182. https://doi.org/10.1016/j.epsl.2019.04.028.

Goddéris, Y., Donnadieu, Y., Le Hir, G., Lefebvre, V., Nardin, E., 2014. The role of palaeogeography in the Phanerozoic history of atmospheric CO2 and climate. Earth Sci. Rev. 128, 122–138. https://doi.org/10.1016/j.earscirev.2013.11.004.

Handoh, I.C., Lenton, T.M., 2003. Periodic mid-Cretaceous oceanic anoxic events linked by oscillations of the phosphorus and oxygen biogeochemical cycles. Glob. Biogeochem. Cycles 17, 1092. https://doi.org/10.1029/2003GB002039.

Haq, B.U., 2014. Cretaceous eustasy revisited. Glob. Planet. Chang. 113, 44–58. https://doi.org/10.1016/j.gloplacha.2013.12.007.

Herrle, J.O., Schröder-Adams, C.J., Davis, W., Pugh, A.T., Galloway, J.M., Fath, J., 2015. Mid-Cretaceous high arctic stratigraphy, climate, and oceanic anoxic events. Geology 43, 403–406. https://doi.org/10.1130/G36439.1.

Hetzel, A., Böttcher, M.E., Wortmann, U.G., Brumsack, H.-J., 2009. Paleo-redox conditions during OAE 2 reflected in Demerara rise sediment geochemistry (ODP Leg 207). Palaeogeogr. Palaeoclimatol. Palaeoecol. 273, 302–328. https://doi.org/10.1016/j.palaeo.2008.11.005.

Jarvis, I., Gale, A.S., Jenkyns, H.C., Pearce, M.A., 2006. Secular variation in Late Cretaceous carbon isotopes: a new δ13C carbonate reference curve for the Cenomanian–Campanian (99.6–70.6 Ma). Geol. Mag. 143, 561–608. https://doi.org/10.1017/S0016756806002421.

Jarvis, I., Lignum, J.S., Gröcke, D.R., Jenkyns, H.C., Pearce, M.A., 2011. Black shale deposition, atmospheric CO2drawdown, and cooling during the Cenomanian-Turonian Oceanic Anoxic Event. Paleoceanography 26, PA3201. https://doi.org/10.1029/2010PA002081.

Jenkyns, H., 1980. Cretaceous anoxic events: from continents to oceans. J. Geol. Soc. Lond. 137, 171–188. https://doi.org/10.1144/gsjgs.137.2.0171.

Jenkyns, H.C., 2003. Evidence for rapid climate change in the Mesozoic–Palaeogene greenhouse world. Philos. Trans. R. Soc. London, Ser. A 361, 1885–1916. https://doi.org/10.1098/rsta.2003.1240.

Jenkyns, H.C., 2010. Geochemistry of oceanic anoxic events. Geochem. Geophys. Geosyst. 11, Q03004. https://doi.org/10.1029/2009GC002788.

Jenkyns, H.C., Dickson, A.J., Ruhl, M., Van den Boorn, S.H., 2017. Basalt-seawater interaction, the Plenus Cold Event, enhanced weathering and geochemical change: deconstructing Oceanic Anoxic Event 2 (Cenomanian–Turonian, Late Cretaceous). Sedimentology 64, 16–43. https://doi.org/10.1111/sed.12305.

Jia, J., Wan, X., Li, G., Chen, H., 2010. Benthic foraminifera as paleoenvironmental indicators and their paleoceanographic significance around the Cenomanian-Turonian boundary in Gamba, Tibet. Acta Micropaleotonlogica Sinica 27, 135–143.

Jones, M.M., Sageman, B.B., Oakes, R.L., Parker, A.L., Leckie, R.M., Bralower, T.J., Sepúlveda, J., Fortiz, V., 2019. Astronomical pacing of relative sea level during Oceanic Anoxic Event 2: preliminary studies of the expanded SH#1 Core, Utah, USA. GSA Bull. 131, 1702–1722. https://doi.org/10.1130/B32057.1.

Jones, M.M., Sageman, B.B., Selby, D., Jicha, B.R., Singer, B.S., Titus, A.L., 2021. Regional chronostratigraphic synthesis of the Cenomanian-Turonian oceanic anoxic event 2 (OAE2) interval, Western Interior Basin (USA): New Re-Os chemostratigraphy and 40Ar/39Ar geochronology. GSA Bull. 133, 1090–1104. https://doi.org/10.1130/B35594.1.

Kalanat, B., Mahmudy-Gharaie, M.H., Vahidinia, M., Vaziri-Moghaddam, H., Kano, A., Kumon, F., 2018. Paleoenvironmental perturbation across the Cenomanian/Turonian boundary of the Kopet-Dagh Basin (NE Iran), inferred from geochemical anomalies and benthic foraminiferal assemblages. Cretac. Res. 86, 261–275. https://doi.org/10.1016/j.cretres.2017.09.019.

Kemp, D.B., Suan, G., Fantasia, A., Jin, S., Chen, W., 2022. Global organic carbon burial during the Toarcian oceanic anoxic event: patterns and controls. Earth Sci. Rev. 231, 104086 https://doi.org/10.1016/j.earscirev.2022.104086.

Kolonic, S., Wagner, T., Forster, A., Sinninghe Damsté, J.S., Walsworth-Bell, B., Erba, E., Turgeon, S., Brumsack, H.J., Chellai, E.H., Tsikos, H., 2005. Black shale deposition on the northwest African Shelf during the Cenomanian/Turonian oceanic anoxic event: climate coupling and global organic carbon burial. Paleoceanography 20, PA1006. https://doi.org/10.1029/2003PA000950.

Komar, N., Zeebe, R.E., 2017. Redox-controlled carbon and phosphorus burial: a mechanism for enhanced organic carbon sequestration during the PETM. Earth Planet. Sci. Lett. 479, 71–82. https://doi.org/10.1016/j.epsl.2017.09.011.

Kraal, P., Slomp, C.P., Forster, A., Kuypers, M.M.M., 2010. Phosphorus cycling from the margin to abyssal depths in the proto-Atlantic during oceanic anoxic event 2. Palaeogeogr. Palaeoclimatol. Palaeoecol. 295, 42–54. https://doi.org/10.1016/j.palaeo.2010.05.014.

Kump, L.R., 1991. Interpreting carbon-isotope excursions: Strangelove oceans. Geology 19, 299–302. https://doi.org/10.1130/0091-7613(1991)019<0299:ICIESO>2.3.CO;2.

Kuypers, M.M., Pancost, R.D., Nijenhuis, I.A., Sinninghe Damsté, J.S., 2002. Enhanced productivity led to increased organic carbon burial in the euxinic North Atlantic basin during the late Cenomanian oceanic anoxic event. Paleoceanography 17, 1051. https://doi.org/10.1029/2000PA000569.

Lenniger, M., Nøhr-Hansen, H., Hills, L.V., Bjerrum, C.J., 2014. Arctic black shale formation during cretaceous Oceanic Anoxic Event 2. Geology 42, 799–802. https://doi.org/10.1130/G35732.1.

Li, X., Jenkyns, H.C., Wang, C., Hu, X., Chen, X., Wei, Y., Huang, Y., Cui, J., 2006. Upper cretaceous carbon-and oxygen-isotope stratigraphy of hemipelagic carbonate facies from southern Tibet, China. J. Geol. Soc. Lond. 163, 375–382. https://doi.org/10.1144/0016-764905-046.

Li, Y.-X., Montanez, I.P., Liu, Z., Ma, L., 2017. Astronomical constraints on global carbon-cycle perturbation during Oceanic Anoxic Event 2 (OAE2). Earth Planet. Sci. Lett. 462, 35–46. https://doi.org/10.1016/j.epsl.2017.01.007.

Londoño, V., Collins, L.S., 2022. Controls on sedimentary accumulation of organic matter during cretaceous Oceanic Anoxic Event 2, IODP site U1407, Southeast Newfoundland Ridge. Mar. Geol. 443, 106699 https://doi.org/10.1016/j.margeo.2021.106699.

Lowery, C.M., Cunningham, R., Barrie, C.D., Bralower, T., Snedden, J.W., 2017. The Northern Gulf of Mexico during OAE2 and the Relationship between Water Depth and Black Shale Development. Paleoceanography 32, 1316–1335. https://doi.org/10.1002/2017PA003180.

Lowery, C.M., Self-Trail, J.M., Barrie, C.D., 2021. Enhanced terrestrial runoff during Oceanic Anoxic Event 2 on the North Carolina Coastal Plain, USA. Clim. Past 17, 1227–1242. https://doi.org/10.5194/cp-17-1227-2021.

Ma, C., Meyers, S.R., Sageman, B.B., Singer, B.S., Jicha, B.R., 2014. Testing the astronomical time scale for oceanic anoxic event 2, and its extension into Cenomanian strata of the Western Interior Basin (USA). GSA Bull. 126, 974–989. https://doi.org/10.1130/B30922.1.

McDonald, B.S., Partin, C.A., Sageman, B., Holmden, C., 2022. Uranium isotope reconstruction of ocean deoxygenation during OAE 2 hampered by uncertainties in fractionation factors and local U-cycling. Geochim. Cosmochim. Acta 331, 143–164. https://doi.org/10.1016/j.gca.2022.05.010.

Meyers, S.R., Siewert, S.E., Singer, B.S., Sageman, B.B., Condon, D.J., Obradovich, J.D., Jicha, B.R., Sawyer, D.A., 2012. Intercalibration of radioisotopic and astrochronologic time scales for the Cenomanian-Turonian boundary interval, Western Interior Basin, USA. Geology 40, 7–10. https://doi.org/10.1130/G32261.1.

Mills, B.J., Donnadieu, Y., Goddéris, Y., 2021. Spatial continuous integration of Phanerozoic global biogeochemistry and climate. Gondwana Res. 100, 73–86. https://doi.org/10.1016/j.gr.2021.02.011.

Monteiro, F.M., Pancost, R.D., Ridgwell, A., Donnadieu, Y., 2012. Nutrients as the dominant control on the spread of anoxia and euxinia across the Cenomanian-Turonian oceanic anoxic event (OAE2): Model-data comparison. Paleoceanography 27, PA4209. https://doi.org/10.1029/2012PA002351.

Mort, H.P., Adatte, T., Keller, G., Bartels, D., Föllmi, K.B., Steinmann, P., Berner, Z., Chellai, E., 2008. Organic carbon deposition and phosphorus accumulation during Oceanic Anoxic Event 2 in Tarfaya, Morocco. Cretac. Res. 29, 1008–1023. https://doi.org/10.1016/j.cretres.2008.05.026.

O'Connor, L.K., Jenkyns, H.C., Robinson, S.A., Remmelzwaal, S.R.C., Batenburg, S.J., Parkinson, I.J., Gale, A.S., 2020. A re-evaluation of the plenus cold event, and the links between CO2, temperature, and seawater chemistry during OAE 2. Paleoceanogr. Paleoclimatol. 35 https://doi.org/10.1029/2019PA003631 e2019PA003631.

Owens, J.D., Gill, B.C., Jenkyns, H.C., Bates, S.M., Severmann, S., Kuypers, M.M., Woodfine, R.G., Lyons, T.W., 2013. Sulfur isotopes track the global extent and dynamics of euxinia during cretaceous Oceanic Anoxic Event 2. Proc. Natl. Acad. Sci. 110, 18407–18412. https://doi.org/10.1073/pnas.1305304110.

Owens, J.D., Lyons, T.W., Hardisty, D.S., Lowery, C.M., Lu, Z., Lee, B., Jenkyns, H.C., 2017. Patterns of local and global redox variability during the Cenomanian–Turonian Boundary Event (Oceanic Anoxic Event 2) recorded in carbonates and shales from central Italy. Sedimentology 64, 168–185. https://doi.org/10.1111/sed.12352.

Owens, J.D., Lyons, T.W., Lowery, C.M., 2018. Quantifying the missing sink for global organic carbon burial during a cretaceous oceanic anoxic event. Earth Planet. Sci. Lett. 499, 83–94. https://doi.org/10.1016/j.epsl.2018.07.021.

Paez-Reyes, M., Carvajal-Ortiz, H., Sahoo, S.K., Varol, O., Miller, B.V., Hughes, G.W., Gaona-Narvaez, T., Patarroyo, G.D., Curtis, J.H., Lerma, I., Copeland, P., 2021. Assessing the contribution of the La Luna Sea to the global sink of organic carbon during the Cenomanian-Turonian Oceanic Anoxic Event 2 (OAE2). Glob. Planet. Chang. 199, 103424 https://doi.org/10.1016/j.gloplacha.2021.103424.

Papadomanolaki, N.M., van Helmond, N.A.G.M., Pälike, H., Sluijs, A., Slomp, C.P., 2022. Quantifying volcanism and organic carbon burial across Oceanic Anoxic Event 2. Geology 50, 511–515. https://doi.org/10.1130/G49649.1.

Paytan, A., McLaughlin, K., 2007. The oceanic phosphorus cycle. Chem. Rev. 107, 563–576. https://doi.org/10.1021/cr0503613.

Pogge von Strandmann, P.A., Jenkyns, H.C., Woodfine, R.G., 2013. Lithium isotope evidence for enhanced weathering during Oceanic Anoxic Event 2. Nat. Geosci. 6, 668–672. https://doi.org/10.1038/ngeo1875.

Poulton, S.W., Henkel, S., März, C., Urquhart, H., Flögel, S., Kasten, S., Sinninghe Damsté, J.S., Wagner, T., 2015. A continental-weathering control on orbitally driven redox-nutrient cycling during cretaceous Oceanic Anoxic Event 2. Geology 43, 963–966. https://doi.org/10.1130/G36837.1.

Prokoph, 2001. Geochronology and calibration of global Milankovitch cyclicity at the Cenomanian-Turonian boundary. Geology 29, 523–526. https://doi.org/10.1130/0091-7613(2001)029<0523:GACOGM>2.0.CO;2.
Redfield, A., Ketchum, B., Richards, F., 1963. The influence of organisms on the composition of seawater. The Sea 2, 26–77.
Rimmer, S.M., Thompson, J.A., Goodnight, S.A., Robl, T.L., 2004. Multiple controls on the preservation of organic matter in Devonian–Mississippian marine black shales: geochemical and petrographic evidence. Palaeogeogr. Palaeoclimatol. Palaeoecol. 215, 125–154. https://doi.org/10.1016/j.palaeo.2004.09.001.
Ruttenberg, K., 2003. The global phosphorus cycle. Treat. Geochem. 8, 585–634. https://doi.org/10.1016/B0-08-043751-6/08153-6.
Sageman, B.B., Meyers, S.R., Arthur, M.A., 2006. Orbital time scale and new C-isotope record for Cenomanian-Turonian boundary stratotype. Geology 34, 125–128. https://doi.org/10.1130/G22074.1.
Schlanger, S., Jenkyns, H., 1976. Cretaceous oceanic anoxic events: causes and consequences. Geol. Mijnb. 55.
Schlanger, S., Arthur, M., Jenkyns, H., Scholle, P., 1987. The Cenomanian-Turonian Oceanic Anoxic Event, I. Stratigraphy and distribution of organic carbon-rich beds and the marine δ13C excursion. Geol. Soc. Lond. Spec. Publ. 26, 371–399. https://doi.org/10.1144/GSL.SP.1987.026.01.24.
Schoepfer, S.D., Shen, J., Wei, H., Tyson, R.V., Ingall, E., Algeo, T.J., 2015. Total organic carbon, organic phosphorus, and biogenic barium fluxes as proxies for paleomarine productivity. Earth Sci. Rev. 149, 23–52. https://doi.org/10.1016/j.earscirev.2014.08.017.
Schröder-Adams, C.J., Herrle, J.O., Selby, D., Quesnel, A., Froude, G., 2019. Influence of the high arctic igneous province on the cenomanian/turonian boundary interval, sverdrup basin, high canadian arctic. Earth Planet. Sci. Lett. 511, 76–88. https://doi.org/10.1016/j.epsl.2019.01.023.
Scotese, C.R., 2016. Tutorial: PALEOMAP paleoAtlas for GPlates and the paleoData plotter program. Paleomap Project Tech. Rep. 56. http://www.earthbyte.org/paleomap-paleoatlas-for-gplates.
Sepúlveda, J., Wendler, J., Leider, A., Kuss, H.-J., Summons, R.E., Hinrichs, K.-U., 2009. Molecular isotopic evidence of environmental and ecological changes across the Cenomanian–Turonian boundary in the Levant Platform of central Jordan. Org. Geochem. 40, 553–568. https://doi.org/10.1016/j.orggeochem.2009.02.009.
Singh, K., Xie, M., 2008. Bootstrap: A Statistical Method. Unpublished manuscript. Rutgers University, USA, pp. 1–14. Retrieved from. http://www.stat.rutgers.edu/home/mxie/RCPapers/bootstrap.pdf.
Takashima, R., Nishi, H., Huber, B.T., Leckie, R.M., 2006. Greenhouse world and the Mesozoic ocean. Oceanography 19, 82–92.
Takashima, R., Nishi, H., Yamanaka, T., Tomosugi, T., Fernando, A.G., Tanabe, K., Moriya, K., Kawabe, F., Hayashi, K., 2011. Prevailing oxic environments in the Pacific Ocean during the mid-cretaceous Oceanic anoxic event 2. Nat. Commun. 2, 234. https://doi.org/10.1038/ncomms1233.
Taylor, S.R., McLennan, S.M., 1985. The Continental Crust: Its Composition and Evolution.
Tessin, A., Hendy, I., Sheldon, N., Sageman, B., 2015. Redox-controlled preservation of organic matter during "OAE 3" within the Western Interior Seaway. Paleoceanography 30, 702–717. https://doi.org/10.1002/2014PA002729.
Trabucho Alexandre, J., Tuenter, E., Henstra, G.A., van der Zwan, K.J., van de Wal, R.S., Dijkstra, H.A., de Boer, P.L., 2010. The mid-Cretaceous North Atlantic nutrient trap: black shales and OAEs. Paleoceanography 25, PA4201. https://doi.org/10.1029/2010PA001925.
Tribovillard, N., Algeo, T.J., Lyons, T., Riboulleau, A., 2006. Trace metals as paleoredox and paleoproductivity proxies: an update. Chem. Geol. 232, 12–32. https://doi.org/10.1016/j.chemgeo.2006.02.012.
Tribovillard, N., Algeo, T., Baudin, F., Riboulleau, A., 2012. Analysis of marine environmental conditions based onmolybdenum–uranium covariation-applications to Mesozoic paleoceanography. Chem. Geol. 324, 46–58. https://doi.org/10.1016/j.chemgeo.2011.09.009.
Tsandev, I., Slomp, C., 2009. Modeling phosphorus cycling and carbon burial during cretaceous Oceanic Anoxic events. Earth Planet. Sci. Lett. 286, 71–79. https://doi.org/10.1016/j.epsl.2009.06.016.
Tsikos, H., Jenkyns, H., Walsworth-Bell, B., Petrizzo, M., Forster, A., Kolonic, S., Erba, E., Silva, I.P., Baas, M., Wagner, T., 2004. Carbon-isotope stratigraphy recorded by the Cenomanian–Turonian Oceanic Anoxic Event: correlation and implications based on three key localities. J. Geol. Soc. Lond. 161, 711–719. https://doi.org/10.1144/0016-764903-077.
Turgeon, S., Brumsack, H.-J., 2006. Anoxic vs dysoxic events reflected in sediment geochemistry during the Cenomanian–Turonian Boundary Event (Cretaceous) in the Umbria–Marche Basin of central Italy. Chem. Geol. 234, 321–339. https://doi.org/10.1016/j.chemgeo.2006.05.008.
Turgeon, S.C., Creaser, R.A., 2008. Cretaceous oceanic anoxic event 2 triggered by a massive magmatic episode. Nature 454, 323–326. https://doi.org/10.1038/nature07076.
van Helmond, N.A., Sluijs, A., Reichart, G.-J., Sinninghe Damsté, J.S., Slomp, C.P., Brinkhuis, H., 2014a. A perturbed hydrological cycle during Oceanic Anoxic Event 2. Geology 42, 123–126. https://doi.org/10.1130/G34929.1.
van Helmond, N.A.G.M., Ruvalcaba Baroni, I., Sluijs, A., Sinninghe Damsté, J.S., Slomp, C.P., 2014b. Spatial extent and degree of oxygen depletion in the deep proto-North Atlantic basin during Oceanic Anoxic Event 2. Geochem. Geophys. Geosyst. 15, 4254–4266. https://doi.org/10.1002/2014GC005528.
Van Helmond, N., Sluijs, A., Sinninghe Damsté, J., Reichart, G.-J., Voigt, S., Erbacher, J., Pross, J., Brinkhuis, H., 2015. Freshwater discharge controlled deposition of Cenomanian–Turonian black shales on the NW European epicontinental shelf (Wunstorf, northern Germany). Clim. Past 11, 495–508. https://doi.org/10.5194/cp-11-495-2015.
Voigt, S., Aurag, A., Leis, F., Kaplan, U., 2007. Late Cenomanian to Middle Turonian high-resolution carbon isotope stratigraphy: New data from the Münsterland cretaceous Basin, Germany. Earth Planet. Sci. Lett. 253, 196–210. https://doi.org/10.1016/j.epsl.2006.10.026.
Wallmann, K., 2010. Phosphorus imbalance in the global ocean? Glob. Biogeochem. Cycles 24, GB4030. https://doi.org/10.1029/2009GB003643.
Wan, X., Wignall, P., Zhao, W., 2003. The Cenomanian–Turonian extinction and oceanic anoxic event: evidence from southern Tibet. Palaeogeogr. Palaeoclimatol. Palaeoecol. 199, 283–298. https://doi.org/10.1016/S0031-0182(03)00543-1.
Wang, C., Hu, X., Jansa, L., Wan, X., Tao, R., 2001. The Cenomanian–Turonian anoxic event in southern Tibet. Cretac. Res. 22, 481–490. https://doi.org/10.1006/cres.2001.0271.
Wang, J., Bulot, L.G., Taylor, K.G., Redfern, J., 2021. Controls and timing of Cenomanian-Turonian organic enrichment and relationship to the OAE2 event in Morocco, North Africa. Mar. Pet. Geol. 128, 105013 https://doi.org/10.1016/j.marpetgeo.2021.105013.
Westermann, S., Vance, D., Cameron, V., Archer, C., Robinson, S.A., 2014. Heterogeneous oxygenation states in the Atlantic and Tethys oceans during Oceanic Anoxic Event 2. Earth Planet. Sci. Lett. 404, 178–189. https://doi.org/10.1016/j.epsl.2014.07.018.
Zhang, X., Chen, K., Hu, D., Sha, J., 2016. Mid-cretaceous carbon cycle perturbations and Oceanic Anoxic events recorded in southern Tibet. Sci. Rep. 6, 39643. https://doi.org/10.1038/srep39643.
Zhang, Y., Benjamin, M., He, T., Yang, T., Zhu, M., 2023. Simulating the long-term carbon cycle in the Phanerozoic: current status and future developments. Chin. Sci. Bull. 68, 1580–1592.